

Effect of vertical stratification on characteristics and energy of nonlinear internal solitary waves from a numerical model



Jieshuo Xie ^{a,b}, Zhiwu Chen ^a, Jiexin Xu ^{a,b}, Shuqun Cai ^{a,*}

^a State Key Laboratory of Tropical Oceanography, South China Sea Institute of Oceanology, CAS, 164 West Xingang Road, Guangzhou 510301, China

^b University of Chinese Academy of Sciences, Beijing 100049, China

ARTICLE INFO

Article history:

Received 3 June 2013

Received in revised form 20 February 2014

Accepted 9 March 2014

Available online 20 March 2014

Keywords:

Nonlinear internal solitary waves

Stratification

Numerical model

Baroclinic energy

South China Sea

ABSTRACT

A numerical model is set up to study the impact of changes in vertical stratification on the properties of internal solitary waves (ISWs) generated by tidal flow over a ridge. Based on modifications of the observed stratification with a secondary thermocline over a main one in the South China Sea, the effects of five kinds of stratification on the characteristics and energy conversion of ISWs are investigated. In general, the isopycnal undergoing maximum displacement below the ridge crest is reduced, the wave amplitude and the number of ISWs in a wave packet increase, while the phase speed, the wave half-width, the sum of ISW kinetic energy (KE) and available potential energy (APE) and the ratio of KE to APE decrease. When the stratification in the upper layer is reduced, the ISW amplitude, the number of ISWs, the phase speed and the sum of KE and APE decrease, while the wave half-width and the ratio of KE to APE increase. If the main thermocline is over the secondary one, the ISW amplitude, the wave half-width, the sum of KE and APE and the ratio of KE to APE increase, while the phase speed reduces. For stratification with two thermoclines, the ISW phase speed increases but the half-width decreases. In addition, the ratio of baroclinic to barotropic energy is found to be between 10% and 40%, and the ratio of ISW KE to APE is between 1.30 and 1.65. It is also shown that the ratio of KE to APE for the stratification with two thermoclines is about 2–6% larger than that for the stratification with only one thermocline. If the thermocline is lowered by about 30 m (0.064 of the total water depth), the ratio of KE to APE reduces by about 10%.

© 2014 Elsevier B.V. All rights reserved.

1. Introduction

In recent decades, oceanic observations of internal solitary waves (ISWs) have often been reported [1–3]. ISWs are usually generated by tidal flow over underwater bathymetry in the stratified ocean. There are several non-dimensional parameters governing the generation of ISWs by tidal flow over underwater ridge. Of the non-dimensional parameters governing the generation of ISWs, most attention has been paid to the relative steepness of topography [4,5],

$$\varepsilon = h_x / \sqrt{(\sigma^2 - f^2)/(N(z)^2 - \sigma^2)}, \quad (1)$$

* Corresponding author. Tel.: +86 20 89023186; fax: +86 20 84451672.

E-mail address: caisq@scsio.ac.cn (S. Cai).

where $h_x = dh/dx$ is the topographic slope, σ is the tidal frequency, f is the Coriolis parameter and $N(z)$ is the buoyancy frequency. According to formula (1), it can be seen that both the structure of stratification and topography are important for governing the generation of ISWs by affecting the relative steepness ε . However, most of the previous work mainly pays attention to the effect of topographic characteristics on ISWs, while the study on the effect of stratification is relatively unexplored.

Actually, a study of the effects of changes in stratification on ISWs is also helpful in understanding the difference of internal wave characteristics in the ocean. For example, on the Caribbean Coast of Puerto Rico, the internal waves have a distinct seasonal variation as the energy conversion from barotropic tides to internal waves is adjusted by the seasonal variation of stratification [6]; in the Bay of Biscay, the excited internal beams get severely distorted due to their scattering in a summer thermocline, which favors the generation of ISWs [7]; in the northern South China Sea (SCS), due to the asymmetry of stratification on both sides of the Luzon Strait, the characteristics of generated ISWs are also different [8]. Moreover, based on the shallow water Korteweg–de Vries (KdV) theory, it can be conjectured that variation in stratification can alter the properties of ISWs [9,10].

There also remains a question regarding the ratio of the wave kinetic energy (KE) to the available potential energy (APE) for a packet of ISWs in different background stratification. For example, observations by Klymak et al. [11] show that, west of the Luzon Strait, the KE is about 40% bigger than the APE for a packet of ISWs; whilst at the Massachusetts Bay, for the nonlinear internal waves before interacting with the bottom topography, the baroclinic energy is thought to be evenly distributed between KE and APE [12]. Theoretically, however, Turkington et al. [13] prove that for exact, fully nonlinear ISWs the KE is always larger than the APE. Based on an accurate formula of APE, Lamb and Nguyen [14] find ratios of KE to APE as high as 30% using quasi-two-layer stratification, and the ratio will increase if the thermocline moves away from the mid-depth. It is also suggested that changes in background stratification influence the conversion of the barotropic-to-baroclinic tide [15].

However, work about the effect of the complex changes in the real oceanic stratification on the ISW characteristic and energy conversion is still relatively unexplored, e.g., the oceanic stratification may have one main thermocline but sometimes two thermoclines, and the depth of thermocline can change largely with time, etc. How do these kinds of variations in vertical stratification affect the ISW characteristic and energy conversion? Thus, a systematic and quantitative study about the effects of different stratification on ISWs is needed. Therefore, an attempt has been made in this paper to study the following two problems. First, how do changes in stratification affect the characteristics of the generated ISWs? Second, how do they affect the partition of the baroclinic energy of ISWs? The full two-dimensional Euler equations model [5], which was employed to the numerical study of the ISWs in the SCS by Xie et al. [16,17], is again used in this study. In the following, the model description, the choice of model parameters and the design of standard stratification are described in Section 2. In Section 3, 9 standard experiments and 140 sensitivity experiments are carried out, and the experimental results are shown and discussed. Finally, the conclusions are summarized in Section 4.

2. Model description and choice of parameters

Considering a two-dimensional (x, z) flow in a stratified ocean, internal waves can be described by the following set of equations,

$$\omega_t + J(\omega, \psi) - f v_z = g \bar{\rho}_x / \bar{\rho}_0 + A^H \omega_{xx} + (A^V \omega_z)_z, \quad (2)$$

$$v_t + J(v, \psi) + f \psi_z = A^H v_{xx} + (A^V v_z)_z, \quad (3)$$

$$\bar{\rho}_t + J(\bar{\rho}, \psi) + \bar{\rho}_0 / g N^2(z) \psi_x = K^H \bar{\rho}_{xx} + (K^V \bar{\rho}_z)_z + (K^V \rho_{0z})_z, \quad (4)$$

$$\omega = \psi_{xx} + \psi_{zz}, \quad (5)$$

where ω is the vorticity, ψ is the streamfunction, $\rho_0(z)$ is the stationary density and $N(z)$ is the corresponding buoyancy frequency, $\bar{\rho}_0$ is a constant average of density, $\bar{\rho}$ is the density disturbance because of the wave motion. The seawater density is written as $\rho(z) = \rho_0(z) + \bar{\rho}(x, z, t)$. (u, v, w) is the velocity vector, $f = 5.07 \times 10^{-5} \text{ s}^{-1}$ is the Coriolis parameter. $A^V = 1 \times 10^{-5} \text{ m}^2 \text{ s}^{-1}$, $A^H = 1 \times 10^{-4} \text{ m}^2 \text{ s}^{-1}$, $K^V = 1 \times 10^{-5} \text{ m}^2 \text{ s}^{-1}$ and $K^H = 1 \times 10^{-4} \text{ m}^2 \text{ s}^{-1}$ are the vertical and horizontal coefficients of turbulent viscosity and mass diffusivity, respectively. J is the Jacobian operator and g is the acceleration due to gravity. It should be noted that the calculation is two-dimensional in the sense that $\partial(\cdot)/\partial y = 0$, but v is present because of the Coriolis force.

The boundary and initial conditions are given as follows,

$$\psi = 0, \quad \omega = 0, \quad v_{\bar{n}} = 0, \quad \bar{\rho}_{\bar{n}} = 0, \quad (z = 0), \quad (6)$$

$$\psi = \psi_0 \sin \sigma t, \quad \omega = 0, \quad v_{\bar{n}} = 0, \quad \bar{\rho}_{\bar{n}} = 0, \quad (z = H(x)), \quad (7)$$

$$\psi = -z \psi_0 \sin(\sigma t) / H_0, \quad \omega = 0, \quad v = -f / \sigma \psi_0 \cos(\sigma t) / H_0, \quad \bar{\rho} = 0, \quad (x = -L), \quad (8)$$

$$\psi = -z\psi_0 \sin(\sigma t)/H_0, \quad \omega = 0, \quad v = -f/\sigma\psi_0 \cos(\sigma t)/H_0, \quad \tilde{\rho} = 0, \quad (x = L) \quad (9)$$

and

$$\psi = 0, \quad \omega = 0, \quad v = -f\psi_0/\sigma/H(x), \quad \tilde{\rho} = 0, \quad (t = 0). \quad (10)$$

Here $z = 0$ means sea surface, $\sigma = 2\pi/T$ is the M_2 tidal frequency ($T = 12.4$ h), ψ_0 is the volume flux for the M_2 barotropic flow and $H(x) = -[H_0 - h_0 \exp(-x^2/2W^2)]$ is the bottom topography of ridge, where $H_0 = 472$ m is the water depth, $h_0 = 235$ m is the height of ridge, and W is the width of ridge which is set as 15 km in the following unless otherwise stated.

In this paper, $U_0 = \psi_0/H_0$ is the amplitude of M_2 tidal current in the deep water which is set as 0.3 m s^{-1} in the following unless otherwise stated, and the computational domain extends from $x = -L$ to L (here L is 250 km). The ISWs are generated by the ridge and propagate away from the source. To simplify the calculation, in the vertical direction, a sigma coordinate transformation in regard to depth is introduced. The thickness of the layer is reduced in the depth intervals with strong stratification by introducing new variables [5],

$$x_2 = x, \quad z_2 = \int_z^0 N(s)ds / \int_{-H(x)}^0 N(s)ds \quad (11)$$

This transformation makes the computation more effective and transforms the irregular calculation area into a rectangle with the vertical variable ranging from 0 to 1. A semi-implicit numerical ADI scheme, which utilizes a rectangular grid with second-order approximations to the spatial derivatives and first-order approximation to the temporal derivatives in every temporal semi-layer, is used to solve the transformed equations. In this paper, the model run is carried out with a horizontal spatial resolution $\Delta x = 100$ m and a time step $\Delta t = 10$ s. The vertical step varies with depth, the number of levels is equal to 60 so that the vertical resolution near the pycnocline is high enough to capture the structure of stratification.

In the following, nine cases of standard stratification based on a typical summer stratification observed in the SCS are designed to study the sensitivity of the generated ISW to changes in stratification. See Table 1 and Fig. 1 for the nine cases. The buoyancy frequency $N(z)$ (Fig. 1a) and the density $\rho_0(z)$ in case C1 are based on the observational data in June, 1998 which recorded the passage of an ISW south of the Donsha Islands [18]. The stratification in case C1 has a secondary thermocline over a main one. The main thermocline appears at a depth of 60 m with a maximum buoyancy frequency of 0.0199 s^{-1} , while the secondary thermocline appears above at a depth of 20 m with a maximum buoyancy frequency of 0.0177 s^{-1} . The buoyancy frequency between the ridge crest and the bottom (at depths between 236 m and 472 m) is about 30–40 times the tidal frequency. The stratification in case C1, which represents a typical oceanic stratification in the northern SCS in summer, is chosen as the standard case for further comparison. Modifications of the stratification in cases C2–C6 are based on case C1. In case C2, the vertical stratification in the lower layer is reduced, i.e., the buoyancy frequency between the ridge crest and the bottom is about 9–27 times the tidal frequency representing the case when the stratification in deep ocean is well mixed. In case C3, the vertical stratification in the upper layer is reduced, with a maximum buoyancy frequency of 0.0182 s^{-1} and 0.0166 s^{-1} at depths of 60 m and 20 m, respectively, which is similar to the weak stratification in winter. In case C4, the positions of the main and secondary thermoclines move about 30 m downward, i.e., the positions of the main and secondary thermoclines are now at 90 m and 50 m, respectively, whilst the stratification strength remains unchanged. In case C5, the positions of the main and secondary thermoclines exchange while the stratification strength remains unchanged, which is also a typical stratification in summer. In case C6, there is only a main thermocline, the secondary one is removed, which is a more typical stratification in the ocean. Modifications of the stratification in cases C7–C9 are based on case C6 which has only one main thermocline: in case C7, the stratification in the lower layer is reduced as in case C2; in case C8, the stratification in the upper layer is reduced as in case C3; in case C9, the position of the main thermocline moves about 30 m downward as in case C4.

According to these cases of stratification, ten pairs of comparative cases which represent five kinds of variations in stratification can be categorized: case pairs (C1, C2) and (C6, C7) have different stratification in the lower layer, case pairs (C1, C3) and (C6, C8) have different stratification in the upper layer, case pairs (C1, C4) and (C6, C9) have different thermocline depths, case pairs (C1, C5) exchange the positions of the main and secondary thermoclines, case pairs (C1, C6), (C2, C7) and (C4, C9)

Table 1
Nine cases of standard stratification.

C1	Observational stratification with a main thermocline under a secondary thermocline
C2	Same as case C1, but the stratification in the lower layer is reduced
C3	Same as case C1, but the stratification in the upper layer is reduced
C4	Same as case C1, but the thermocline is lowered
C5	Same as case C1, but the main and secondary thermoclines exchange their positions
C6	Stratification with only a main thermocline, i.e., the secondary thermocline in case C1 is removed
C7	Same as case C6, but the stratification in the lower layer is reduced
C8	Same as case C6, but the stratification in the upper layer is reduced
C9	Same as case C6, but the thermocline is lowered

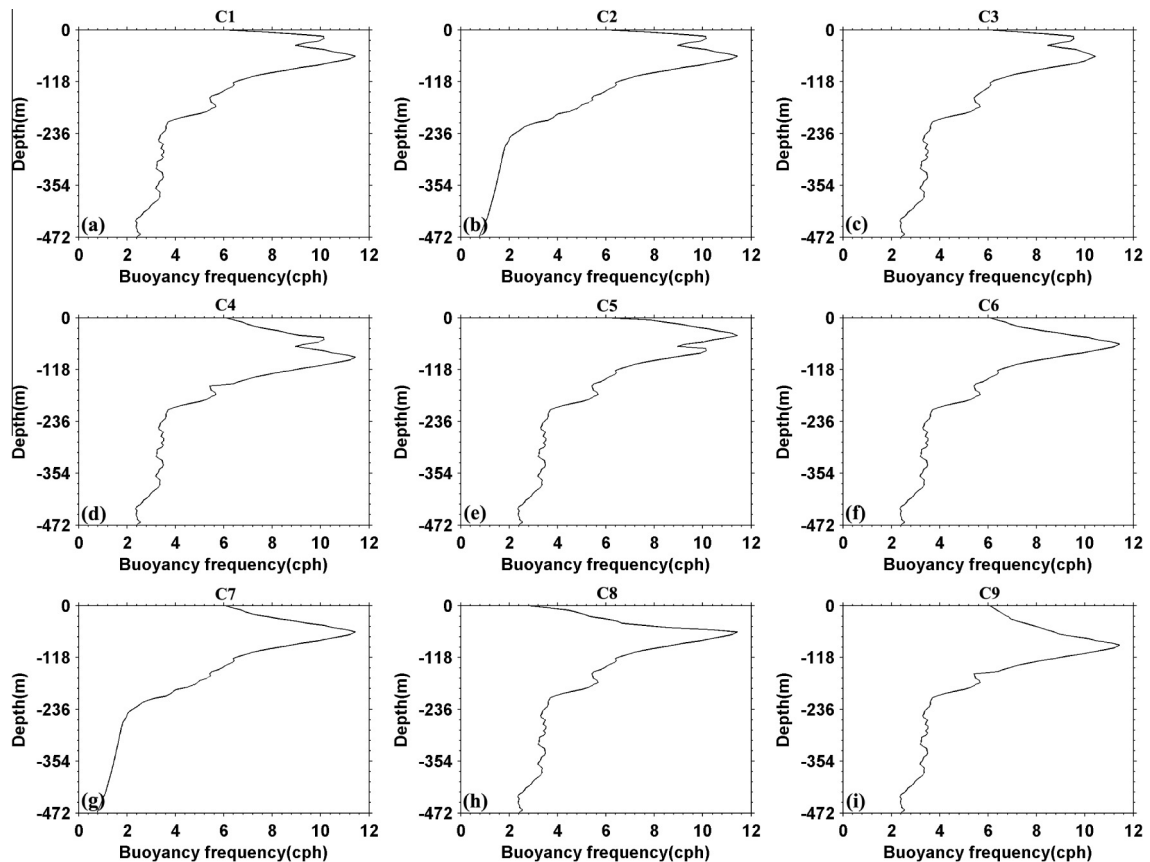


Fig. 1. Vertical distribution of buoyancy frequencies, $N(z)$, in nine standard cases as described in Table 1. The stratification in case C1 is based on the observation in the South China Sea.

contrast stratification with two thermoclines and one thermocline. In the following, the effect of variations in stratification on the generated ISWs is studied by comparisons among these five kinds of comparative cases.

3. Numerical experiments results and discussion

In this section, 9 standard experiments corresponding to the different stratification cases from C1 to C9, respectively, are carried out, and another 138 sensitivity experiments with a wide variation range of model input parameters are designed to investigate the sensitivity of model results. See Tables 2 and 5 for more details. The experiments CiE1 (here $i = 1-9$) are chosen as the standard experiments for detailed analyses and further comparisons. For each experiment, the model is run continuously for 8 tidal periods and the data from the fourth period are saved for analysis. Since the simulated results are almost symmetric across the ridge, only results in the right half of the model domain are considered. Fig. 2 shows the density fields at the fourth tidal period in experiments CiE1 ($i = 1-9$), where the dashed line denotes the location of the leading ISW trough in the first wave packet. In the following, we first only describe the main results from the standard experiment C1E1 in Section 3.1, since Xie et al. [17] have validated that the simulated ISW induced current in experiment C1E1 agrees well with the synchronous observational one. The conclusions of the effects of changes in stratification on the properties of generated ISWs are presented in Section 3.2. In Section 3.3, the 138 sensitivity experiments results are analyzed, and discussion is presented in Section 3.4.

3.1. Standard experiment C1E1

The characteristics of the wave amplitudes, the number of ISWs, the wave half-width and the energy conversion, etc. of ISWs in the well-developed leading packet in experiment C1E1 are summarized in Table 3 and shown in Figs. 2a, 3–5. The ISW amplitude in experiment C1E1 is 44.07 m, which appears at a depth of $D = -95$ m (i.e., 0.20 of the total depth). The number of ISWs in a wave packet is about 7 or 8. The leading ISW of the first generated ISW packet is about 167.91 km far away from the ridge with a phase speed, c , of about 1.53 m/s. The variation of the vertical isopycnal displacements with

Table 2

Numerical experiments, which include 9 standard experiments and 126 sensitivity experiments with a wide variation range of tidal forcing or ridge width. Note: Ci ($i = 1-9$) represents 9 standard stratification cases. The two parameters within each bracket in the second column represent the tidal forcing U_0 (m s^{-1}) and the ridge width W (km), respectively. CiE1 ($i = 1-9$) represents 9 standard experiments with the same tidal forcing $U_0 = 0.3 \text{ m s}^{-1}$ and ridge width $W = 15.0 \text{ km}$; CiUj ($i = 1-9$; $j = 1-8$) represents 72 sensitivity experiments with different tidal forcings; CiWj ($i = 1-9$; $j = 1-6$) represents 54 sensitivity experiments with different ridge widths.

Standard stratification cases		C1	C2	C3	C4	C5	C6	C7	C8	C9
Standard experiments	E1 (0.30, 15.0)	C1E1	C2E1	C3E1	C4E1	C5E1	C6E1	C7E1	C8E1	C9E1
Tidal current strength sensitivity experiments with a wide range of tidal forcing U_0 from 0.15 m s^{-1} to 0.55 m s^{-1}	U1 (0.15, 15.0)	C1U1	C2U1	C3U1	C4U1	C5U1	C6U1	C7U1	C8U1	C9U1
	U2 (0.20, 15.0)	C1U2	C2U2	C3U2	C4U2	C5U2	C6U2	C7U2	C8U2	C9U2
	U3 (0.25, 15.0)	C1U3	C2U3	C3U3	C4U3	C5U3	C6U3	C7U3	C8U3	C9U3
	U4 (0.35, 15.0)	C1U4	C2U4	C3U4	C4U4	C5U4	C6U4	C7U4	C8U4	C9U4
	U5 (0.40, 15.0)	C1U5	C2U5	C3U5	C4U5	C5U5	C6U5	C7U5	C8U5	C9U5
	U6 (0.45, 15.0)	C1U6	C2U6	C3U6	C4U6	C5U6	C6U6	C7U6	C8U6	C9U6
	U7 (0.50, 15.0)	C1U7	C2U7	C3U7	C4U7	C5U7	C6U7	C7U7	C8U7	C9U7
	U8 (0.55, 15.0)	C1U8	C2U8	C3U8	C4U8	C5U8	C6U8	C7U8	C8U8	C9U8
Topography sensitivity experiments with a wide range of ridge width W ranges from 5 km to 15 km	W1 (0.30, 5.0)	C1W1	C2W1	C3W1	C4W1	C5W1	C6W1	C7W1	C8W1	C9W1
	W2 (0.30, 7.5)	C1W2	C2W2	C3W2	C4W2	C5W2	C6W2	C7W2	C8W2	C9W2
	W3 (0.30, 10.0)	C1W3	C2W3	C3W3	C4W3	C5W3	C6W3	C7W3	C8W3	C9W3
	W4 (0.30, 12.5)	C1W4	C2W4	C3W4	C4W4	C5W4	C6W4	C7W4	C8W4	C9W4
	W5 (0.30, 17.5)	C1W5	C2W5	C3W5	C4W5	C5W5	C6W5	C7W5	C8W5	C9W5
	W6 (0.30, 20.0)	C1W6	C2W6	C3W6	C4W6	C5W6	C6W6	C7W6	C8W6	C9W6

Table 3

Characteristics and energy conversion of ISWs in experiments CiE1 ($i = 1-9$).

Experiments	ISW amplitude η_0 (m)	Depth of max. displacement $D(\text{m})/\frac{D}{H_0}$	Number of ISWs	Location of ISWs (km)	Phase speed of ISWs $c(\text{m s}^{-1})/c_0 - 1$	Total energy of APE and KE (MJ m^{-1})	Ratio of KE and APE (KE/APE)
C1E1	-44.07	-95/0.20	7-8	167.91	1.53/0.13	145.7	1.53
C2E1	-45.68	-85/0.18	9-10	161.51	1.47/0.15	123.3	1.50
C3E1	-37.51	-100/0.21	5-6	159.77	1.45/0.09	122.9	1.62
C4E1	-51.67	-105/0.22	7-8	185.56	1.68/0.12	215.1	1.44
C5E1	-47.02	-95/0.20	6-7	166.08	1.51/0.14	151.8	1.56
C6E1	-44.49	-100/0.21	7-8	166.83	1.51/0.12	143.0	1.51
C7E1	-45.92	-95/0.20	9-10	160.41	1.46/0.15	122.1	1.46
C8E1	-44.24	-100/0.21	5-6	163.47	1.50/0.12	143.2	1.55
C9E1	-51.14	-110/0.23	7-8	182.53	1.65/0.12	208.9	1.42

depth through the centre of the leading ISW is shown in Fig. 3a, the solid line refers to the model result and the dashed line refers to that of the mode-one wave by calculation of the normal modes [19,20]. It can be seen that the modeled depth of the isopycnal undergoing maximum displacement is nearer to the main thermocline than that calculated by the normal modes. Theoretically, the ratio of the amplitude of j th soliton to that of the leading soliton in a rank-ordered ISW packet can be expressed as $\gamma = \frac{\eta_j}{\eta_1} = \left(\frac{M-j}{M-1}\right)^2$ [21], where M represents the number of ISWs in a wave packet, η_1 represents the amplitude of the leading ISW and η_j represents the amplitude of j th ISW. Fig. 3b shows both the modeled and theoretical amplitude ratios γ of experiment C1E1. It can be seen that, the modeled amplitude of 2nd ISW in one wave packet is $0.67\eta_1$, which is smaller than the theoretically predicted value ($0.74\eta_1$); however, the modeled amplitudes of 3rd, 4th and 5th ISWs are larger than those theoretically predicted. The relation between wave half-width, L_w , and wave amplitude, η_0 , can be

Table 4

Effects of changes in stratification on the characteristics and energy conversion of the generated ISWs (note that the symbol '+'/'-' denotes an increase/decrease of the parameters, whilst the blank denotes no significant variation).

Variation of the vertical stratification	ISW amplitude	Depth of isopycnal undergoing max. displacement	Number of ISWs	Wave half-width	Phase speed	Total energy of APE and KE	Ratio of KE to APE (KE/APE)
Stratification in the lower layer reduces: experiment pairs (C1E1,C2E1) or (C6E1,C7E1)	+	–	+	–	–	–	–
Stratification in the upper layer reduces: experiment pairs (C1E1,C3E1) or (C6E1,C8E1)	–	+	–	+	–	–	+
Thermocline is lowered: experiment pairs (C1E1,C4E1) or (C6E1,C9E1)	+	+		+	+	+	–
Stratification with a main thermocline over a secondary thermocline: experiment pairs (C1E1,C5E1)	+			+	–	+	+
Stratification with only one main thermocline: experiment pairs (C1E1,C6E1), (C2E1,C7E1) or (C4E1,C9E1)		+		+	–		–

Table 5

12 Sensitivity experiments with a wide variation range of stratification. C1Rj ($j = 1-6$) represents 6 experiments with different stratification at depth from $-H_0$ to $-H_0/3$ based on the standard experiment C1E1 with two thermoclines; C6Rj ($j = 1-6$) represents 6 experiments with different stratification at depth from $-H_0$ to $-H_0/3$ based on the standard experiment C6E1 with only one thermocline.

Stratification changed at depth from $-H_0$ to $-H_0/3$	R1	R2	R3	R4	R5	R6
Stratification sensitivity experiments based on standard experiment C1E1	C1R1	C1R2	C1R3	C1R4	C1R5	C1R6
Stratification sensitivity experiments based on standard experiment C6E1	C6R1	C6R2	C6R3	C6R4	C6R5	C6R6

theoretically expressed as $L_w = \sqrt{\frac{4h_1^2 h_2^2}{3\eta_0(h_2 - h_1)}}$ [21], here h_1 and h_2 are the water depths of upper and lower layers, respectively. Fig. 3c is the variation of wave half-width with ISW amplitude for the leading five rank-ordered ISWs. Both the numerical and theoretical results show that the wave half-width decreases with amplitude; however, the wave half-width predicted by the numerical simulation is larger than that by the theoretical analysis, which may be due to the broadening property of ISWs in the fully nonlinear numerical model [22].

The wave APE and KE in a closed finite domain are calculated by the following formulas,

$$\text{APE} = \int_{x_l}^{x_r} \int_{-H(x)}^0 E_a dz dx \quad (12)$$

and

$$\text{KE} = \int_{x_l}^{x_r} \int_{-H(x)}^0 E_k dz dx, \quad (13)$$

where E_a is the available potential energy density and E_k is the kinetic energy density [23], and $x_r - x_l$ denotes an integration distance across a well-developed wave packet. The available potential energy density E_a is defined as,

$$E_a(x, z, t) = g \int_z^{z^*} (\bar{\rho}(s) - \rho(x, z, t)) ds, \quad (14)$$

where $z^*(x, z, t)$ is the height of the fluid parcel at (x, z) at time t in the reference state, and $\bar{\rho}$ is the initial undisturbed density [23]. The time-averaged barotropic and baroclinic energy densities provide a measure of the energy available for mixing and the contribution from barotropic and baroclinic motions to mixing [24,25]. Here, the tidally averaged APE and KE densities are defined as,

$$\bar{E}_a(x, z) = \frac{1}{T} \int_t^{t+T} E_a(x, z, t) dt \quad (15)$$

and

$$\bar{E}_k(x, z) = \frac{1}{T} \int_t^{t+T} E_k(x, z, t) dt, \quad (16)$$

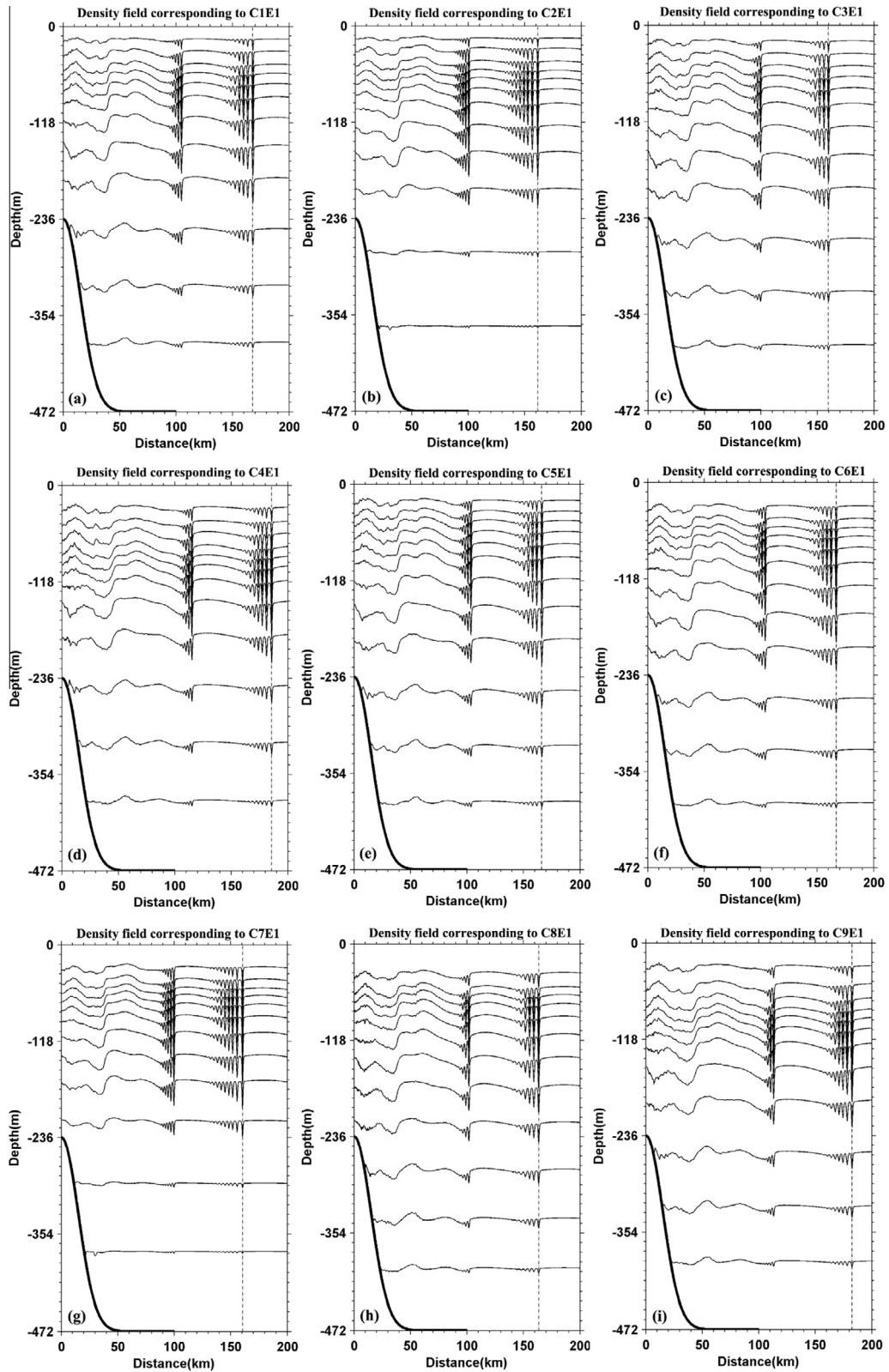


Fig. 2. Distribution of the density field after running four tidal periods in experiments C1E1 ($i = 1-9$), respectively (where the dashed line denotes the location of the trough of leading ISW in the first wave packet).

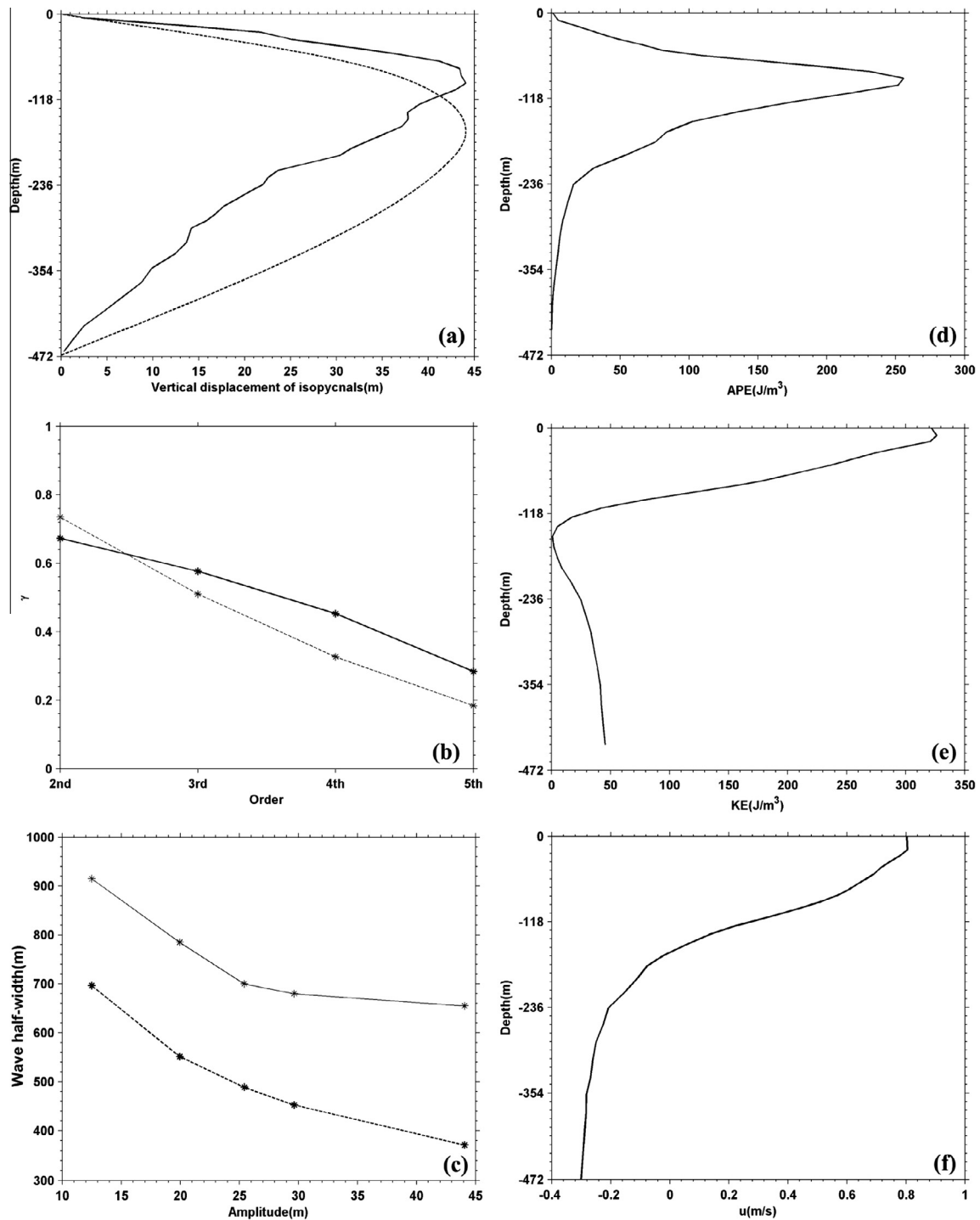


Fig. 3. Results in experiment C1E1. (a) Variation of the vertical displacement of isopycnals with depth along the dashed line denoted in Fig. 2a (where the solid line is the numerical result and the dashed line is that of mode-one wave by calculation of normal modes [20]); (b) ratio of j th ISW amplitude to that of the leading ISW one in the first wave packet (where the solid line is the numerical result and the dashed line is the theoretical solution [19]); (c) variation of ISW half-widths with amplitudes of the leading five rank-ordered ISWs in the first wave packet (where the solid line is the numerical result and the dashed line is the theoretical analysis [20]); (d) and (e) are the APE and KE densities vs. depth along the dashed line section denoted in Fig. 2a, respectively; (f) variation of horizontal current velocity with depth along the dashed line section denoted in Fig. 2a.

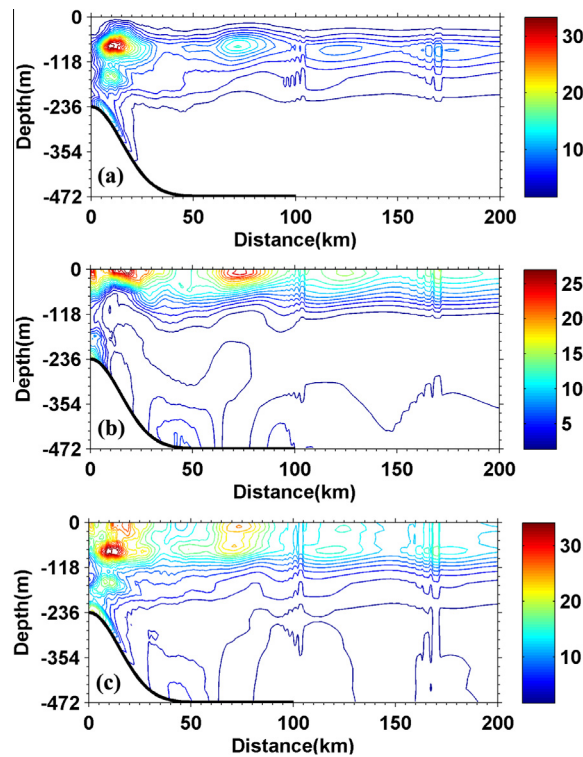


Fig. 4. Tidally averaged baroclinic energy density (in unit of J/m^3) in experiment C1E1. (a) APE, (b) KE, and (c) total baroclinic energy.

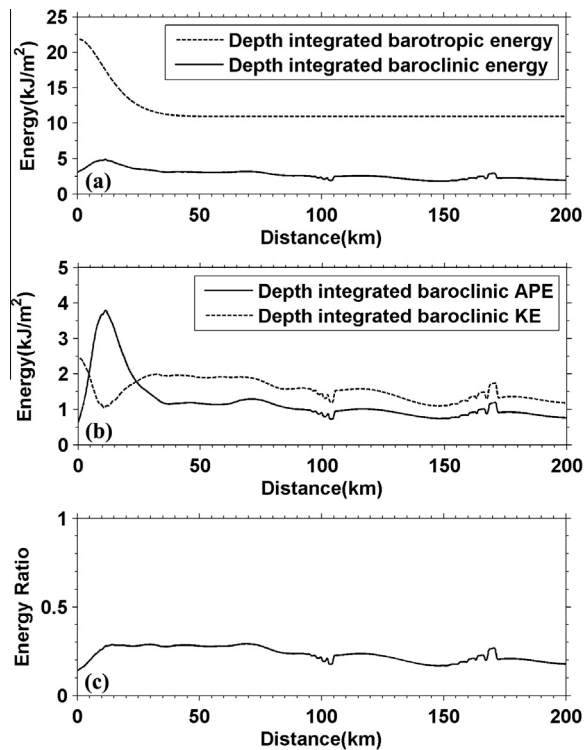


Fig. 5. (a) Tidally averaged depth integrated barotropic and baroclinic energy, (b) tidally averaged depth integrated baroclinic APE and KE, and (c) ratio of the tidally averaged baroclinic to barotropic energy.

respectively [8,26]. The time-averaged energy is calculated within 200 km from the ridge crest, and from $t = 4T$ to $t = 5T$, the calculated averaged energy is saved every $T/280$ for further analysis.

Distribution of the wave APE and KE densities vs. depth along the dashed lines in Fig. 2 is shown in Fig. 3d and e, which can also be implied in distributions of vertical displacements of isopycnals (Fig. 3a) and horizontal current velocity (Fig. 3f) vs. depth, respectively. According to formulas (12) and (13), the computed wave APE and KE in the first ISW packet is about 57.7 MJ/m and 88.0 MJ/m, respectively. Thus, the ratio of wave KE to APE is about 1.53 and the total baroclinic energy density is about 145.7 MJ/m. The tidally averaged APE, KE and total baroclinic energy density are shown in Fig. 4. It can be seen that the baroclinic wave energy is generally excited in the upper layer above the ridge, and then it radiates away from the ridge.

Fig. 5a shows the tidally averaged depth integrated barotropic and baroclinic energy within 200 km from the ridge crest. Because the numerical model uses a rigid lid approximation, only the barotropic kinetic energy is calculated to estimate the barotropic energy, and the baroclinic energy is defined as the sum of the APE and KE. It can be seen that the maximum barotropic energy with a value of $\sim 22 \text{ kJ m}^{-2}$ appears right on the top of ridge. Moving away from the ridge it decreases and finally becomes constant off the ridge. This is reasonable, since in the constant depth region of the domain the barotropic energy is presumably only kinetic energy which depends on time, thus the depth integrated tidally averaged barotropic energy is constant off the ridge. In contrast, the maximum tidally averaged baroclinic energy ($\sim 4.9 \text{ kJ m}^{-2}$) appears about 11.4 km away from the ridge where the slope is the greatest. The depth integrated tidally averaged baroclinic APE and KE are shown in Fig. 5b. It can be seen that the maximum tidally averaged baroclinic KE ($\sim 2.4 \text{ kJ m}^{-2}$) also appears above the ridge crest, while the maximum APE is larger ($\sim 3.8 \text{ kJ m}^{-2}$) and occurs $\sim 11.3 \text{ km}$ away from the ridge. The wave APE is generally larger than the wave KE near the ridge; however, about 25 km from the ridge, the APE is equal to the KE, and beyond that location, the KE is larger. This suggests that, near the ridge, the baroclinic energy generally exists in the form of APE, while in the far field, a part of APE converts into the baroclinic KE when ISWs propagate away from the ridge, therefore the ISW KE is larger ($\text{KE/APE} = 1.53$). Fig. 5b and c also show oscillations in the baroclinic energy, baroclinic APE and KE

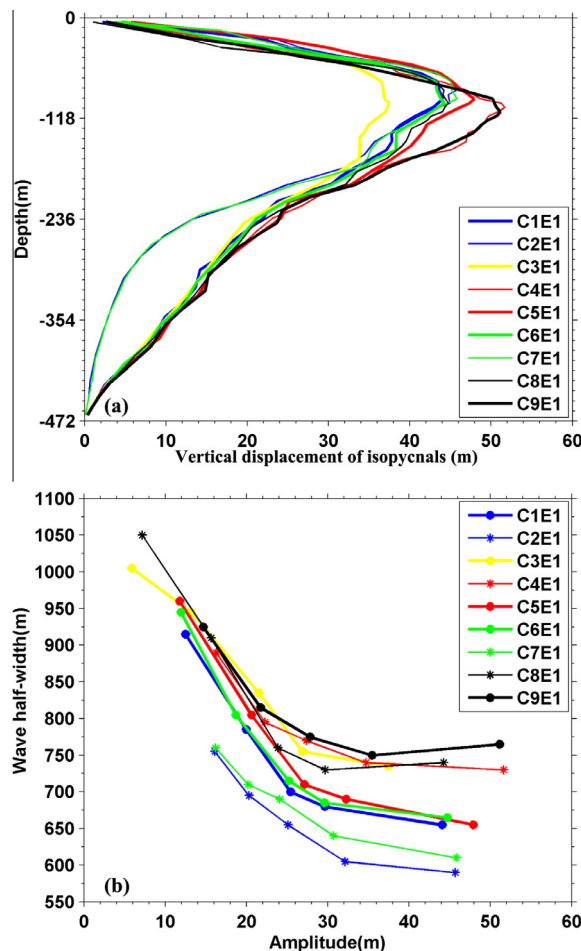


Fig. 6. Comparison of the model results in experiments CiE1 ($i = 1-9$). (a) Vertical displacements of isopycnals vs. depth along the dashed line section denoted in Fig. 2, and (b) variation of ISW half-widths with amplitudes of the leading five rank-ordered ISWs in the first wave packet.

at the locations of ISW packets off the ridge, since even in the constant depth region of the domain, the tidal period is different from the passage period of ISWs, thus the depth integrated tidally averaged baroclinic energy oscillates at the locations of ISW packets off the ridge due to the nonlinear effect. The oscillations of the baroclinic energy for ISWs off the ridge are different from the constant baroclinic energy for internal tides off the ridge [26]. Fig. 5c shows the ratio of baroclinic to barotropic energy, which is about 15–30%. It can be seen that, near the ridge crest, the ratio of baroclinic to barotropic energy is the least, while away from the ridge, this ratio increases. Our modeled result would be compared with that by Wunsch [24] who suggested that the ratio of baroclinic to barotropic energy density for internal tides was from 10% to 50%, and this ratio also had a wide and unsystematic geographic variation.

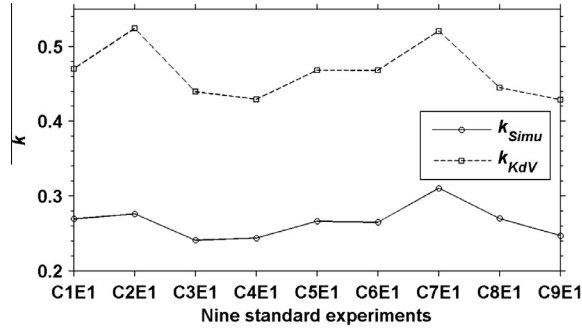


Fig. 7. Value k , defined as $k = \frac{c/c_0 - 1}{\eta_0/D}$, for the nine standard experiments. Solid line: model simulation; dashed line: KdV theory.

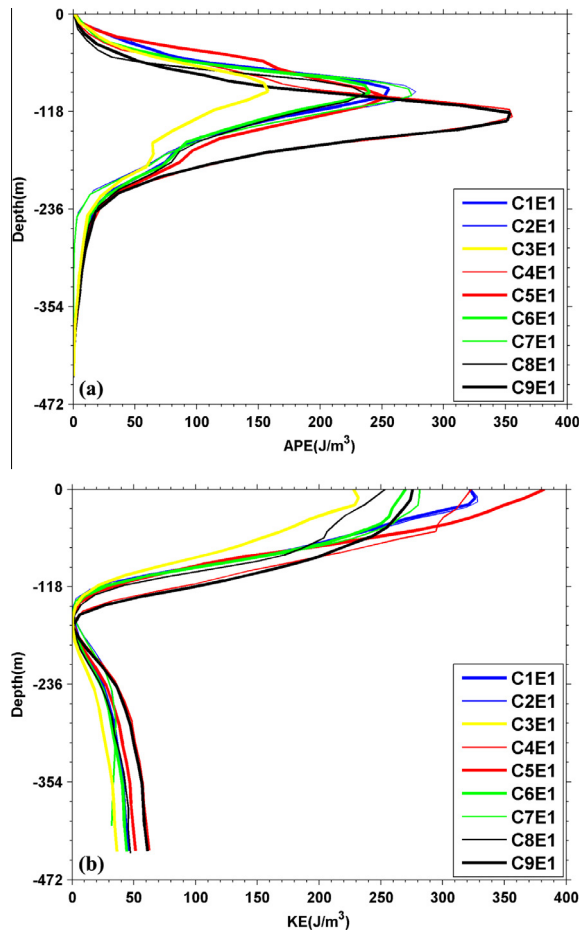


Fig. 8. Same as in Fig. 3d and e but for experiments CiE1 ($i = 1-9$).

3.2. Comparison of results among the standard experiments CiE1 ($i = 1-9$)

In this subsection, the effects of changes in stratification on the characteristics and energy conversion of generated ISWs are discussed by comparing the results among the standard experiments CiE1 ($i = 1-9$) (Table 1). The density fields of the generated ISWs corresponding to experiments C2E1–C9E1 are shown in Fig. 2b–i, and information on the wave amplitude, the energy conversion and the wave half-width, etc. is provided in Table 3 and Figs. 6–9.

According to the results in Table 3 and Fig. 6a, it is obviously that the isopycnal undergoing maximum displacement in ISWs is about 25–40 m below the main thermocline. By comparison among experiments CiE1 ($i = 1-9$), it can be seen that: (1) for the stratification with only one main thermocline, the depth of the isopycnal undergoing maximum displacement is deeper than that with two thermoclines, e.g., compare experiments C1E1 with C6E1, C2E1 with C7E1 and C4E1 with C9E1; (2) the reduction of stratification in the lower layer increases the ISW amplitude and results in the depth of the isopycnal undergoing maximum displacement being nearer to the main thermocline, e.g., compare experiments C1E1 with C2E1 and C6E1 with C7E1; (3) if the thermocline is lowered, the ISW amplitude increases and the depth of the isopycnal undergoing maximum displacement becomes deeper, e.g., compare experiments C1E1 with C4E1 and C6E1 with C9E1; (4) when the main and secondary thermoclines exchange their positions, the ISW amplitude with the main thermocline over the secondary one is larger, e.g., compare experiments C1E1 with C5E1; and (5) if the stratification in the upper layer is reduced, the ISW amplitude decreases, e.g., compare experiments C1E1 with C3E1 and C6E1 with C8E1. The effects of changes in stratification on the ISW amplitude and depth of the isopycnal undergoing maximum displacement are summarized in Table 4.

The number of the generated ISWs is also provided in Table 3. It is found that, (1) the reduction of stratification in the lower layer increases the number of ISWs, e.g., compare experiments C1E1 with C2E1 and C6E1 with C7E1; and (2) the reduction of the stratification in the upper layer reduces the number of ISWs, e.g., compare experiments C1E1 with C3E1 and C6E1 with C8E1.

The variation of ISW amplitude with wave half-width of the five rank-ordered waves in the leading wave packet in each experiment is shown in Fig. 6b. Similar to that in experiment C1E1, in experiments C2E1–C9E1, the wave half-width also

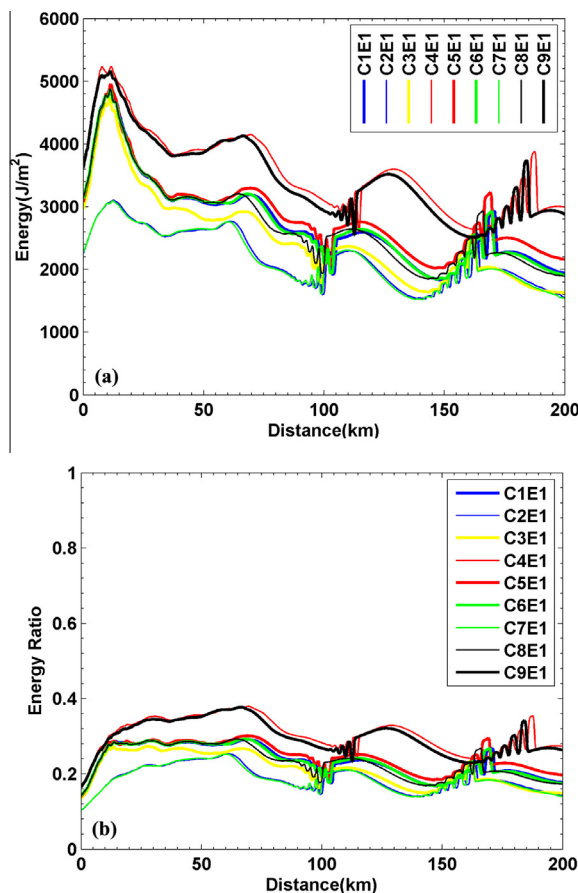


Fig. 9. Comparison of the model results in experiments CiE1 ($i = 1-9$). (a) Tidally averaged depth integrated baroclinic energy, (b) ratio of the tidally averaged baroclinic to barotropic energy.

decreases with wave amplitude when the wave amplitude is small, but it starts to increase with wave amplitude when the wave amplitude gets larger (e.g., in experiments C8E1 and C9E1). In fact, this is the characteristic of the fully nonlinear ISWs which has also been shown by Warn-Varnas et al. [8]. By comparison among experiments C1E1 ($i = 1-9$), it can also be seen that: (1) for the stratification with only one main thermocline, the wave half-width is larger than that with two thermoclines, e.g., compare experiments C1E1 with C6E1, C2E1 with C7E1 and C4E1 with C9E1; (2) the reduction of stratification in the lower layer reduces the wave half-width, e.g., compare experiments C1E1 with C2E1 and C6E1 with C7E1, and vice versa, the reduction of stratification in the upper layer increases the wave half-width, e.g., compare experiments C1E1 with C3E1 and C6E1 with C8E1; (3) if the thermocline is lowered, the wave half-width increases, e.g., compare experiments C1E1 with C4E1 and C6E1 with C9E1; and (4) when the main and secondary thermoclines exchange their positions, the wave half-width with the main thermocline over the secondary one is larger, e.g., compare experiments C1E1 with C5E1. The results of the stratification effects on the number of ISWs and wave half-width are also summarized in Table 4.

Theoretically the phase speed of ISW increases with amplitude [21,27]. According to the resulted locations and phase speeds, c , of the ISWs in Table 3, it is reasonable to see that the ISWs propagate farther if the phase speeds are larger. It is also found that: (1) for the stratification with only one main thermocline, the phase speed is smaller than that with two thermoclines, e.g., compare experiments C1E1 with C6E1, C2E1 with C7E1 and C4E1 with C9E1; (2) the reduction of stratification in the upper or lower layer reduces the phase speed, e.g., compare experiments C1E1 with C2E1, C6E1 with C7E1, C1E1 with C3E1 and C6E1 with C8E1; (3) if the thermocline is lowered, the phase speed increases, e.g., compare experiments C1E1 with C4E1 and C6E1 with C9E1; and (4) when the main and secondary thermoclines exchange their positions, the phase speed with the main thermocline over the secondary one is smaller, e.g., compare experiments C1E1 with C5E1. The effects of changes in stratification on the ISW phase speeds are also summarized in Table 4. Moreover, similar to [22], the relationship between the phase speed, c , and amplitude, η_0 , expressed as $k = \frac{c/c_0 - 1}{\eta_0/D}$ is compared with that derived from the weakly nonlinear KdV theory, where D represents the depth with the maximum ISW displacements. The difference of the simulated results k_{simu} from those derived from the KdV theory k_{KdV} is shown in Fig. 7. It can be seen that $k_{KdV} > k_{simu}$ for all of the nine standard stratification cases, which is also in agreement with the properties of the fully nonlinear ISWs [22]. Besides, it is found that, when the thermocline is lowered, the phase speed for the leading ISW increases by about 10%, which agrees well with the model results by Warn-Varnas et al. [8].

In the following, we focus on effect of changes in stratification on the energy conversion of generated ISWs. Fig. 8 shows the vertical distribution of the wave APE and KE densities vs. depth along the vertical dashed line through the leading waves shown in Fig. 2 in all experiments. The distribution of the wave KE or APE density is consistent with the property of the first mode ISW. It is clearly that the wave KE and APE densities converted from the tidal current are sensitive to the changes in stratification. Table 3 provides the total wave APE and KE in one packet of ISWs. It can be seen that: (1) for the stratification with only one main thermocline, the ratio of KE to APE reduces, e.g., compare experiments C1E1 with C6E1, C2E1 with C7E1 and C4E1 with C9E1; (2) if the thermocline is lowered, the sum of KE and APE increases while the ratio of KE to APE decreases, e.g., compare experiments C1E1 with C4E1 and C6E1 with C9E1; (3) the reduction of the stratification in the lower layer reduces the sum of KE and APE and the ratio of KE to APE, e.g., compare experiments C1E1 with C2E1 and C6E1 with C7E1; (4) the reduction of the stratification in the upper layer increases the ratio of KE to APE, e.g., compare experiments C1E1 with C3E1 and C6E1 with C8E1; and (5) when the main and secondary thermoclines of the stratification exchange their positions, the stratification with the main thermocline over the secondary one increases the sum of KE and APE and the ratio of KE to APE, e.g., compare experiments C1E1 with C5E1. The impact of changes in stratification on the conversion of baroclinic energy is also summarized in Table 4. Further, it is found that the ISW KE is about 40–60% bigger than APE, which is close to the estimation based on the observed stratification west of the Luzon Strait by Klymak et al. [11] and is higher than that based on a theoretical quasi-two-layer stratification by Lamb and Nguyen [14]. Moreover, it can be seen that if the thermocline is lowered, the sum of KE and APE can increase by up to 46%, which is comparable to a value of ~34% implied by Warn-Varnas et al. [8] (see their Table 4 for cases 6 and 7).

The averaged depth integrated baroclinic energy and the ratio of baroclinic to barotropic energy in all experiments are shown in Fig. 9, respectively. It can be seen that the ratio ranges from 10% to 40% depending on different stratification. During the ISW generation process (within about 25 km away from the ridge crest), it is found that: (1) the reduction of the stratification in the lower layer reduces the conversion of barotropic-to-baroclinic energy, e.g., compare experiments C1E1 with C2E1, C6E1 with C7E1; (2) if the thermocline is lowered, the conversion of barotropic-to-baroclinic energy increases, e.g., compare experiments C1E1 with C4E1 and C6E1 with C9E1; and (3) the other changes in stratification have no significant effect on the conversion of barotropic-to-baroclinic energy. According to the results in experiments C1E1 (denoted by thick blue line) and C3E1 (denoted by thick yellow line) in Fig. 9a, it can be seen that in the generation process (within about 25 km away from the ridge crest) the baroclinic energy of ISWs is basically the same, while in the propagation process it is dependent on the stratification.

3.3. Sensitivity of baroclinic energy to a wide range of input parameters

In order to further confirm the conclusions in the paper, another 138 experiments are run to test the sensitivity of the baroclinic energy in the generated ISWs to a wide variation range of input parameters (e.g., tidal forcing, topography and stratification). The sensitivity of the baroclinic energy in one packet of ISWs to a wide variation range of tidal forcing is

shown in Fig. 10 (see Table 2 for 72 sensitivity experiments with different tidal forcings). In each case, nine experiments with tidal forcing U_0 ranging from 0.15 m s^{-1} to 0.55 m s^{-1} are carried out. It can be seen that, the sum of KE and APE in all of the stratification cases increases with the strength of tidal forcing, and the increasing rate is relatively larger if the thermocline is lowered (e.g., cases C4 and C9). Moreover, it is found that, in a wide variation range of tidal forcing, the sum of KE and APE is not very sensitive to the existence of the secondary thermocline, but the ratio of KE to APE is more sensitive to it (e.g., compare cases C1 with C6, C2 with C7 and C4 with C9).

Fig. 11 shows the sensitivity of the baroclinic energy in one packet of ISWs to a wider variation range of topography. See Table 2 for the 54 sensitivity experiments with different ridge widths. In each case, seven experiments with the ridge width W ranging from 5 km to 20 km are carried out. Here, only the ridge width is adjusted, so that the maximum relative steepness of topography, ε_{\max} , ranges from 0.3 to 1.5. According to Fig. 11, it can be seen that, in all of the nine cases, the

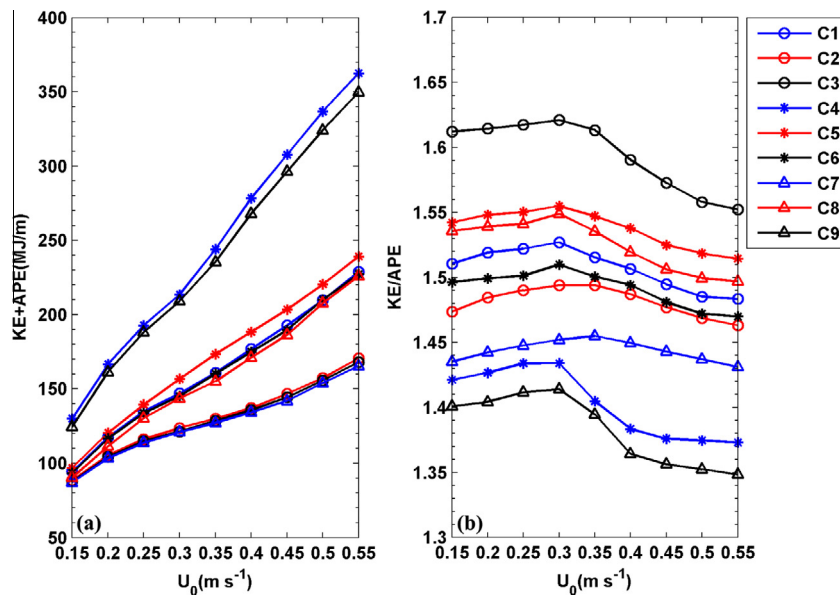


Fig. 10. Variation of baroclinic energy with tidal forcing U_0 . In each stratification case C_i ($i = 1-9$), nine experiments including C_{iE1} and C_{iUj} ($j = 1-8$) are carried out with tidal forcing U_0 ranging from 0.15 m s^{-1} to 0.55 m s^{-1} . (a) Sum of KE and APE, (b) ratio of KE to APE.

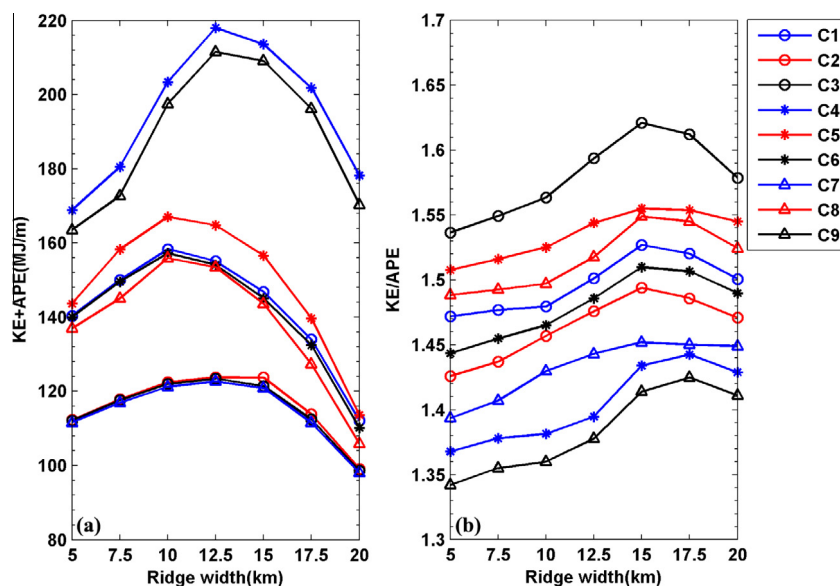


Fig. 11. Variation of baroclinic energy with ridge width W . In each stratification case C_i ($i = 1-9$), seven experiments including C_{iE1} and C_{iWj} ($j = 1-6$) are carried out with ridge width W ranging from 5 km to 20 km. (a) Sum of KE and APE, (b) ratio of KE to APE.

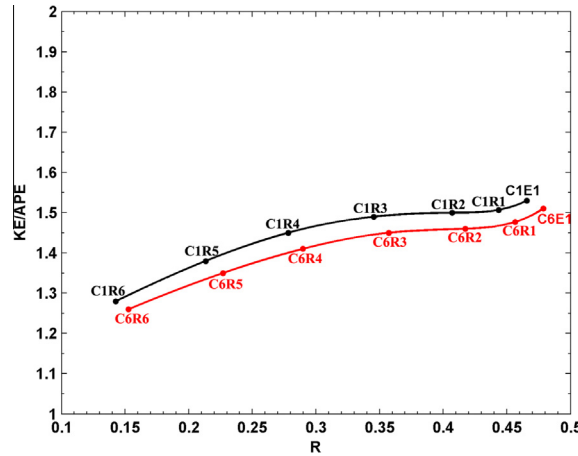


Fig. 12. Variation of ratio of KE to APE with weight of stratification at depth from $-H_0$ to $-H_0/3$. The black color curve represents the stratification with two thermoclines in experiments C1Rj ($j = 1-6$), and the red color one represents that with only one thermocline in experiments C6Rj ($j = 1-6$). (For interpretation of the references to colour in this figure legend, the reader is referred to the web version of this article.)

sum of wave KE and APE gets maximum near the critical value of relative steepness (i.e., $0.5 < \varepsilon_{\max} < 1$, which corresponds to the ridge width W ranging from 10 km to 15 km). In addition, when the relative steepness of ridge slope is supercritical (i.e., $\varepsilon_{\max} > 1$, which corresponds to $W < 10$ km), the sum of wave KE and APE decreases since much of the baroclinic energy is converted into the higher mode internal waves which are easily dissipated near the ridge. Moreover, similar to the sensitivity analysis of tidal forcing, it can be seen that, the sum of KE and APE is also not very sensitive to the existence of the secondary thermocline in a wide variation range of topography, but the ratio of KE to APE is more sensitive to it.

It can also be seen that, in a wide variation range of tidal forcing and topography, the ratio of KE to APE in experiments with two thermoclines is always about 2–6% larger than that with only one thermocline (e.g., compare cases C1 with C6, C2 with C7 and C4 with C9 in Figs. 10b and 11b). If the thermocline is lowered by about 30 m (i.e., 0.064 of the total depth), the ratio of KE to APE reduces by 10% (e.g., compare cases C1 with C4 and C6 with C9 in Figs. 10b and 11b). Further, according to the resulted ratio of KE to APE in Figs. 10b and 11b, it is found that the maximum ratio appears at a moderate tidal forcing ($0.25 \text{ m s}^{-1} < U_0 < 0.35 \text{ m s}^{-1}$) or a relative steepness ($0.3 < \varepsilon_{\max} < 0.6$, which is corresponding to the ridge width W ranging from 12.5 km to 17.5 km), and the ratio of KE to APE is about 1.30–1.65.

In the following, 12 sensitivity experiments are run to investigate the sensitivity of the ratio of KE to APE to a wide variation range of stratification. First, a parameter R is defined as $R = \int_{-H_0}^{-H_0/3} N(z) dz / \int_{-H_0}^0 N(z) dz$, which represents the weight of stratification at depth from $-H_0$ to $-H_0/3$. 12 sensitivity experiments are designed by changing the stratification in the standard experiments C1E1 and C6E1, respectively, at depth from $-H_0$ to $-H_0/3$, so that the strength of stratification vs. depth varies with R ranging from 0.13 to 0.48. See Table 5 and Fig. 12 for details of the 12 sensitivity experiments. In Fig. 12, the black and red color curves represent the experiments with different stratification based on the standard experiments C1E1 and C6E1, respectively. It can be seen that, in a wide variation range of stratification, the ratio of KE to APE with two thermoclines is always about 5% larger than that with only one thermocline. It is also found that the ratio of KE to APE decreases as R is reduced. It is noted that, when $R < 0.2$, the stratification in experiments C1R6 and C6R6 is close to the quasi-two-layer stratification [14], and the resulted ratios of KE to APE in experiments C1R6 and C6R6 are close to 1.3, which is in agreement with the conclusion in [14].

3.4. Discussion

The conclusions obtained in Sections 3.2 and 3.3 are helpful in understanding some of the seasonal activity of the ISWs on the Caribbean coast of Puerto Rico [6], in the Bay of Biscay [7], in the Lake Constance [28] and even in the SCS [29]. E.g., the monthly SAR-observed ISW occurrence frequencies in the SCS show that high frequencies are distributed from April to July with a maximum occurrence frequency of 20% in June, and the low occurrence frequencies are distributed from December to February with a minimum occurrence frequency of 1.5% in February. Actually, the structures of stratification in summer and spring are quite different from those in autumn and winter due to the seasonal variations of solar radiation, latent and sensible heat fluxes in the SCS [30]. The conclusions in this study show that the seasonal variation of vertical stratification structures may be an important factor for the seasonal variation of ISWs in the SCS. By comparison between experiment pairs (C1E1, C3E1) or (C6E1, C8E1), it is found that the reduction of stratification in the upper layer reduces the number of ISWs and the ISW amplitude, thus the oceanic surface signatures of ISWs in the SCS are weaker and fewer in winter. However, it is shown that the possible factors for the seasonal variation of ISWs in world's ocean are different and complex [7,30], and this

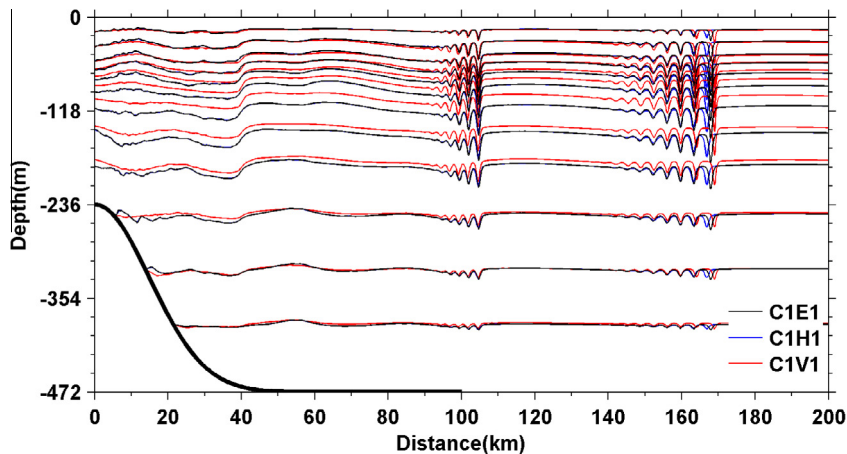


Fig. 13. Comparison of the simulated density fields in experiments C1E1, C1H1 and C1V1.

would require a sustained long-term ocean observing system, e.g., at least similar to Liu and Weisberg [31], which is needed for the insightful understanding of the seasonal activity of ISWs in the SCS.

Finally, based on the standard experiment C1E1, we carry out two more experiments in which the values of viscosity and diffusivity coefficients A^V , A^H , K^V and K^H are changed to test the sensitivity of the numerical results to subgrid mixing: in one experiment (C1H1) the horizontal coefficients of viscosity/diffusivity are increased to $1 \text{ m}^2 \text{ s}^{-1}$, while in the other experiment (C1V1) the vertical coefficients of viscosity/diffusivity are increased to $1 \times 10^{-2} \text{ m}^2 \text{ s}^{-1}$. It is found that some difference exists due to the variation of eddy viscosity/diffusivity, e.g., Fig. 13 shows the comparison of the simulated density fields in these two experiments with that in the standard experiment C1E1. In experiment C1H1, when the horizontal coefficients of viscosity/diffusivity is increased largely, the modeled leading ISW amplitude ($\sim 36.1 \text{ m}$) decreases by about 18.2% and the leading ISW falls behind about 1.03 km with respect to experiment C1E1; whilst in experiment C1V1, when the vertical coefficients of viscosity/diffusivity is increased largely, the modeled leading ISW amplitude ($\sim 49.3 \text{ m}$) increases by about 11.9% and the leading ISW exceeds in distance about 1.01 km with respect to experiment C1E1. Thus, these viscosity and diffusivity coefficients should be carefully chosen in numerical modeling because the simulated characteristics of ISWs are sensitive to the intensity of subgrid mixing.

4. Summary and conclusions

The generation and propagation of ISWs are sensitive to changes in strength and vertical structure of stratification. In this paper, a total of 149 experiments are run to study the impacts of changes in stratification on ISWs generated by tidal flow over a ridge. The standard stratification used in the model is based on observation in the SCS, and eight more cases of stratification are obtained by modifying the base stratification by combinations of: (i) reducing the stratification above/below the thermocline; (ii) moving the thermocline to a greater depth; (iii) removing the secondary thermocline and (iv) switching the locations of the main and secondary thermoclines. The analyses are focused on the properties of ISWs, the kinetic and available potential energy, and the ratio of baroclinic to barotropic energy.

In general, the isopycnal undergoing maximum displacement in ISWs is from slightly below the main thermocline. It is found that, the depth of the isopycnal undergoing maximum displacement decreases if the stratification in the lower layer is reduced, whilst it increases if the stratification in the upper layer is reduced, or the thermocline is lowered, or the secondary thermocline is removed.

When the stratification in the lower layer is reduced, the ISW amplitude and the number of ISWs increase, whilst the wave half-width, the ISW phase speed, the sum of KE and APE and the ratio of KE to APE reduce. When the stratification in the upper layer is reduced, the wave half-width and the ratio of KE to APE increase, while the ISW amplitude, the number of ISWs, the phase speed and the sum of KE and APE reduce. If the position of the thermocline is lowered, the ISW amplitude, the wave half-width, the ISW phase speed and the sum of KE and APE increase. For stratification with two thermoclines, the ISW phase speed increases but the wave half-width decreases. Finally, if the main thermocline is over the secondary one, the ISW amplitude, the wave half-width, the sum of KE and APE and the ratio of KE to APE increase, while the phase speed reduces. The ratio of baroclinic to barotropic energy is found to be between 10% and 40%, and the ratio of ISW KE to APE for the oceanic stratification is between 1.30 and 1.65. The sensitivity results to a wide range of model input parameters show that the ratio of KE to APE for the stratification with two thermoclines is about 2–6% larger than that for the stratification with only one thermocline. If the thermocline is lowered by about 30 m, the ratio of KE to APE reduces

by about 10%. Moreover, the maximum of the ratio of KE to APE in all of the stratification cases appears at a moderate tidal forcing or relative steepness.

Although the effects of changes in stratification on the properties of ISWs generated by tidal flow over a ridge are investigated here, further work is still needed. First, the thermocline assumed here lies above the mid-depth of the water column, however, the thermocline may be below the mid-depth of water in shallow sea where elevation ISWs are common. Second, only the effects of changes in stratification on mode-1 ISWs are studied, whilst those effects on mode-2 ISWs as reported in [16,32–34] are ignored here. Third, the model used here is two-dimensional in the sense that $\partial(\cdot)/\partial y = 0$, thus the important three-dimensional effect on the ISWs [35] cannot be shown. Fourth, a constant Coriolis parameter f is assumed in this study, while the dynamical property of ISWs might be somewhat different if f is changed [5].

Acknowledgments

Many insightful and constructive comments from two anonymous reviewers greatly help improve this paper and are gratefully acknowledged. This work was jointly supported by the Strategic Priority Research Program of the Chinese Academy of Sciences (No. XDA11020201), the National Basic Research Program (Nos. 2011CB013701 and 2013CB956101), the Knowledge Innovation Program of the Chinese Academy of Sciences (Nos. SQ201302 and LTOZZ1304) and NSFC Grant No. 41025019. Jieshuo Xie was also partially supported by a grant from the Research Grants Council of the Hong Kong, Special Administrative Region, China (CUHK 402912).

References

- [1] Liu AK, Chang YS, Hsu MK, Liang NK. Evolution of nonlinear internal waves in East and South China Seas. *J Geophys Res* 1998;103:7995–8008.
- [2] Zhao Z, Alford M. Source and propagation of internal solitary waves in the northeastern South China Sea. *J Geophys Res* 2006;111:C11012.
- [3] Da Silva JCB, New AL, Magalhaes JM. Internal solitary waves in the Mozambique channel: observations and interpretation. *J Geophys Res* 2009;114:C05001.
- [4] Garrett C, Kunze E. Internal tide generation in the deep ocean. *Annu Rev Fluid Mech* 2007;39:57–87.
- [5] Vlasenko V, Stashchuk N, Hutter K. Baroclinic tides: theoretical modeling and observational evidence. Cambridge, UK: Cambridge University Press; 2005. 351 pp.
- [6] Giese GS, Chapman DC, Black PG, Fornshell JA. Causation of large-amplitude coastal seiches on the Caribbean coast of Puerto Rico. *J Phys Oceanogr* 1990;20:1449–58.
- [7] Gerkema T, Lam FPA, Maas LRM. Internal tides in the Bay of Biscay: conversion rates and seasonal effects. *Deep Sea Res II* 2004;51:2995–3008.
- [8] Warn-Varnas A, Hawkins J, Lamb KG, Piacsek S, Chin-Bing S, Burgos G. Solitary wave generation dynamics at Luzon strait. *Ocean Model* 2010;31:9–27.
- [9] Helfrich KR, Melville WK. Long nonlinear internal waves. *Annu Rev Fluid Mech* 2006;38:395–425.
- [10] Grimshaw RH, Pelinovsky E, Talipova T. Modeling internal solitary waves in the coastal ocean. *Surv Geophys* 2007;28:273–98.
- [11] Klymak JM, Pinkel R, Liu CT, Liu AK, David L. Prototypical solitons in the South China Sea. *Geophys Res Lett* 2006;33:L11607.
- [12] Scotti A, Beardsley R, Butman B. On the interpretation of energy and energy fluxes of nonlinear internal waves: an example from Massachusetts Bay. *J Fluid Mech* 2006;561:103–12.
- [13] Turkington B, Eydeland A, Wang S. A computational method for solitary internal waves in a continuously stratified fluid. *Stud Appl Math* 1991;85:93–127.
- [14] Lamb KG, Nguyen VT. Calculating energy flux in internal solitary waves with an application to reflectance. *J Phys Oceanogr* 2009;39:559–80.
- [15] Shroyer EL, Moum JN, Nash JD. Nonlinear internal waves over New Jersey's continental shelf. *J Geophys Res* 2011;116:C03022.
- [16] Xie J, Cai S, He Y. A continuously stratified nonlinear model for internal solitary waves in the northern South China Sea. *Chin J Oceanol Limnol* 2010;28(5):1040–8.
- [17] Xie J, Xu J, Cai S. A numerical study of the load on cylindrical piles exerted by internal solitary waves. *J Fluids Struct* 2011;27:1252–61.
- [18] Cai S, Gan Z, Long X. Some characteristics and evolution of the internal soliton in the northern South China Sea. *Chin Sci Bull* 2002;47(1):21–6.
- [19] Apel JR, Ostrovsky LA, Stepanyants YA, Lynch JF. Internal solitons in the ocean. Technical, Report 2006; WHOI-2006-04.
- [20] Cai S, Long X, Wu R, Wang S. Geographical and monthly variability of the first baroclinic Rossby radius of deformation in the South China Sea. *J Mar Syst* 2008;74:711–20.
- [21] Osborne AR, Burch TL. Internal solitons in the Andaman Sea. *Science* 1980;208:451–60.
- [22] Grue J, Jensen A, Rusås P, Kristian SJ. Properties of large-amplitude internal waves. *J Fluid Mech* 1999;380:257–78.
- [23] Lamb KG. On the calculation of the available potential energy of an isolated perturbation in a density stratified fluid. *J Fluid Mech* 2008;597:415–27.
- [24] Wunsch C. Internal tides in the ocean. *Rev Geophys* 1975;13(1):167–82.
- [25] Dushaw BD, Cornuelle BD, Worcester PF, Howe BM, Luther DS. Barotropic and baroclinic tides in the central North Pacific Ocean determined from long range reciprocal acoustic transmissions. *J Phys Oceanogr* 1995;25:631–47.
- [26] Holloway PE, Merrifield MA. Internal tide generation by seamounts, ridges, and islands. *J Geophys Res* 1999;104(C11):25937–51.
- [27] Choi W, Camassa R. Fully nonlinear internal waves in a two-fluid system. *J Fluid Mech* 1999;396:1–36.
- [28] Preusse M, Freistühler H, Peeters F. Seasonal variation of solitary wave properties in Lake Constance. *J Geophys Res* 2012;117:C04026.
- [29] Zheng Q, Susanto RD, Ho CR, Song YT, Xu Q. Statistical and dynamical analyses of generation mechanisms of solitary internal waves in the northern South China Sea. *J Geophys Res* 2007;112:C03021.
- [30] Huang W, Johannessen J, Alpers W, Yang J, Gan X. Spatial and temporal variations of internal wave sea surface signatures in the northern South China Sea studied by spaceborne SAR imagery. *Process in SeaSAR 2008*; Frascati, Italy, January 21–25, pp. 1–6, ESA SP-656.
- [31] Liu Y, Weisberg RH. Seasonal variability on the West Florida Shelf. *Prog Oceanogr* 2012;104:80–98.
- [32] Vlasenko V, Alpers W. Generation of secondary internal waves by the interaction of an internal solitary wave with an underwater bank. *J Geophys Res* 2005;110:C02019.
- [33] Shroyer EL, Moum JN, Nash JD. Mode 2 waves on the continental shelf: ephemeral components of the nonlinear internal wavefield. *J Geophys Res* 2010;115:C07001.
- [34] Yang YJ, Fang YC, Chang MH, Ramp SR, Kao CC, Tang TY. Observations of second baroclinic mode internal solitary waves on the continental slope of the northern South China Sea. *J Geophys Res* 2009;114:C10003.
- [35] Cai S, Xie J. A propagation model for the internal solitary waves in the northern South China Sea. *J Geophys Res* 2010;115:C12074.